Volume 11 | Number 19 | 21 May 2019 | Pages 9219–9782

Nanoscale

rsc.li/nanoscale

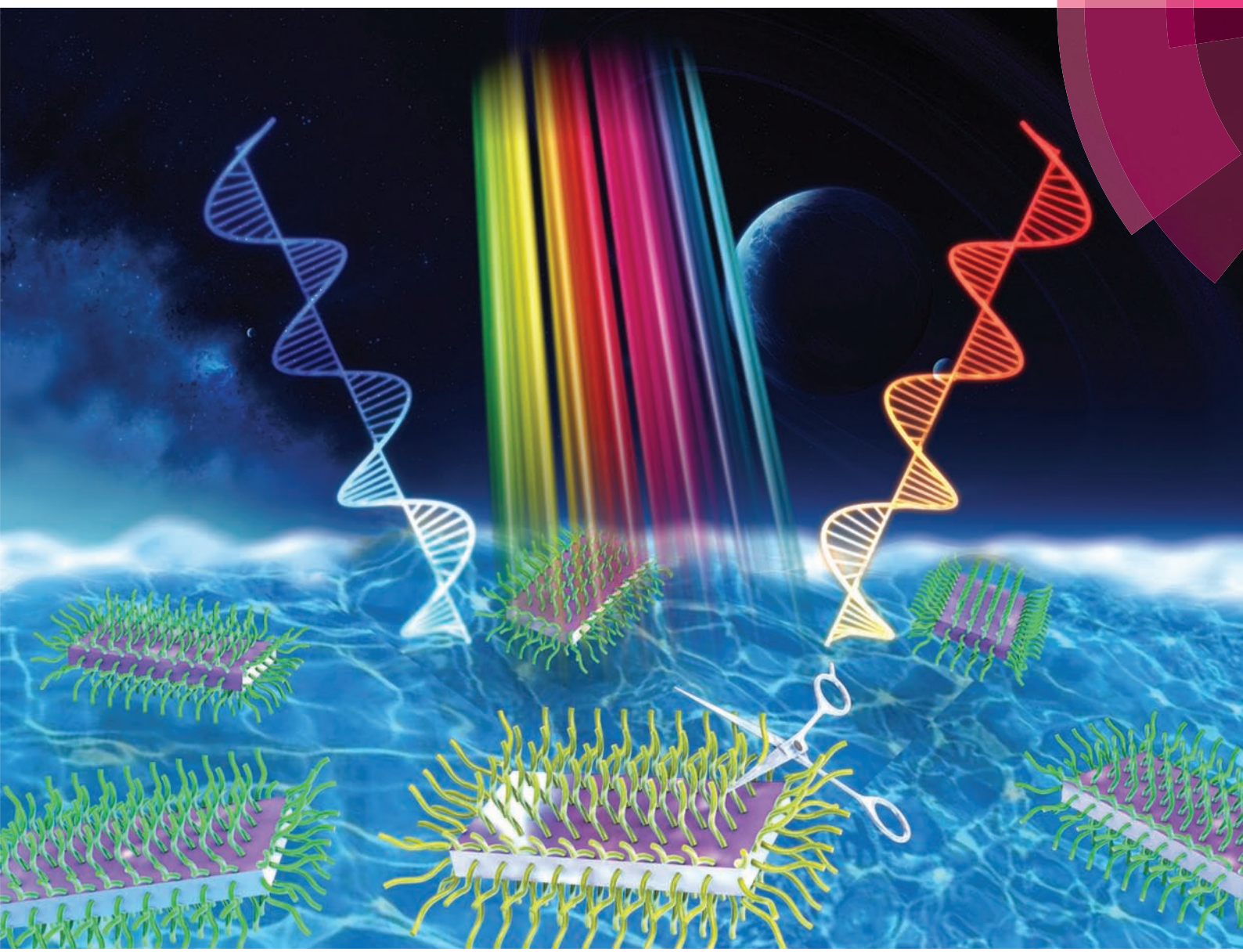

ISSN 2040-3372

ROYAL SOCIETY OF CHEMISTRY | Celebrating IYPT 2019

PAPER
Marie-Hélène Delville, Tingchao He, Rui Chen *et al.*
Chiral CdSe nanoplatelets as an ultrasensitive probe for lead ion sensing

NCNST

Nanoscale

PAPER

Cite this: *Nanoscale*, 2019, **11**, 9327

Chiral CdSe nanoplatelets as an ultrasensitive probe for lead ion sensing†

Xiongbin Wang,‡[a] Junjie Hao,‡[a,b] Jiaji Cheng, ‡[c,d] Junzi Li,[c] Jun Miao,[e,f] Ruxue Li,[a] Yiwen Li,[a,e] Jiagen Li,[g] Yuhui Liu,[a] Xi Zhu,[g] Yanjun Liu, [a] Xiao Wei Sun, [a] Zikang Tang,[e] Marie-Hélène Delville,*[b] Tingchao He *[c] and Rui Chen *[a]

Received 29th December 2018,
Accepted 5th March 2019

DOI: 10.1039/c8nr10506e

rsc.li/nanoscale

As opposed to traditional photoluminescence and ultra-violet based optical sensing, we present here a sensing system based on resolved optically active polarization with promising applications. It is based on the ultrathin CdSe nanoplatelets (NPLs) when modified with either L or D-cysteine molecules (L/D-cys) as bio-to-nano ligands. The chiral ligand transfers its chiroptical activity to the achiral nanoplatelets with an anisotropy factor of ~10^{-4}, which unlocks the chiral excitonic transitions and allows lead ion detection with a limit of detection (LOD) as low as 4.9 nM. Simulations and modelling based on time-dependent density functional theory (TD-DFT) reveal the chiral mechanism of L/D-cys capped CdSe NPLs. The presented CD-based sensing system illustrates an alternative possibility of using chiral CdSe NPLs as competitive chiral sensors for heavy metal ion detection.

Introduction

Colloidal semiconductor nanoparticles (NPs) with chirality have attracted tremendous interest due to their unique electronic and optical properties, which open the floodgate for novel sensitive chiroptical platforms as compared to their pristine achiral counterparts.[1–13] Generally, the induction of chirality in semiconductor NPs can be classified as: (i) NPs with intrinsically chiral dislocations and defects,[14–17] (ii) chiral surfaces formed by chiral ligands or chiral interactions between chiral ligands and an achiral semiconductor core,[18–21] and (iii) chiral assemblies consisting of achiral nanocrystals.[22–27] For instance, G. Markovich's group has accomplished an enantioselective synthesis of intrinsically chiral mercury sulfide NPs.[17] More recently, N. A. Kotov *et al.*[28] reported the preparation of chiral tungsten oxide hydrate NPs with chirality transferred from the chiral ligands proline (Pro) and aspartic acid (Asp) to the tungsten oxide NPs *via* bio-to-nano chirality transfer. Such NPs can facilitate the formation of peptide bonds, leading to Asp-Asp and Asp-Pro dipeptides. Moreover, M. Liu and his colleagues reported the synthesis of chiral assembled perovskite nanostructures through a supramolecular self-assembly approach and perovskite NPs with circularly polarized luminescence (CPL) were successfully synthesized.[29] However, semiconductor NPs with intrinsic chirality or assembled chiral geometries often suffer from laborious chemical procedures or sophisticated fabrication processes, leading to large scale, high cost and time-consuming production. Currently, the most universal method is the chirality transfer which is based on the electronic interactions between chiral molecules and the achiral semiconductor core. As a result, intriguing circular dichroism (CD) peaks occur in the vicinity of the absorption bands of the colloidal NPs.[30] Recently, chiral ligand capped semiconductor nanodots,[31–34] nanorods[19,35] and NPLs[36–39] as well as their core–shell nanostructures have been extensively studied. Like in the case of metallic plasmonic NPs such as Au or Ag, the strong coupling between the chiral ligand and the achiral semiconductor can induce subsequent chirality transfer from molecules to the semiconductor core with an anisotropic factor close to 10^{-4}.[2,4,40–42] Such an emerging property can be easily tuned by a simple control of the size, composition and shapes of the semiconductor NPs. Therefore, it could provide great potential for applications in chiral catalysis,[18,43] stereoselective synthesis,[17,44] and more importantly, in chiral sensing.[45–49]

[a]*Department of Electrical and Electronic Engineering, Southern University of Science and Technology, Shenzhen, Guangdong, 518055, P. R. China. E-mail: chenr@sustech.edu.cn*
[b]*University of Bordeaux, CNRS, ICMCB, UMR 5026, F-33608 Pessac, France. E-mail: marie-helene.delville@icmcb.cnrs.fr*
[c]*College of Physics and Energy, Shenzhen University, Shenzhen, Guangdong, 518060, P. R. China. E-mail: tche@szu.edu.cn*
[d]*School of Materials Science and Engineering, Hubei University, Wuhan 430062, P. R. China*
[e]*The Institute of Applied Physics and Materials Engineering, University of Macau, Avenida da Universidade, Taipa, Macau, Macao*
[f]*Department of Materials Science and Engineering, Southern University of Science and Technology, Shenzhen, Guangdong, 518055, P. R. China*
[g]*School of Science and Engineering, The Chinese University of Hong Kong, Guangdong, 518172, P. R. China*
† Electronic supplementary information (ESI) available. See DOI: 10.1039/c8nr10506e
‡ These authors contributed equally to this work.

Heavy metal ions in water significantly affect human health and global environments. It is necessary to develop reliable and low-cost methods with high sensitivity for their detection as well as remediation. The most utilized approach for heavy metal ion detection up-to-now has been fluorescence-based color probing, during which semiconductor NPs would undergo emission quenching with the introduction of heavy metal ions.[50–56] These ions exfoliate capping ligands around the semiconductor NPs, interact with their surface and generate a photoluminescence "on–off" sensing detectable by a colorimetric method. However, such a fluorescence detection strategy suffers from limitations such as the lack of specificity of the fluorescent carrier materials and their relatively low sensitivity in water. However, using the emerging chirality in semiconductor NPs induced by capping ligands could be a suitable alternative for a fast and accurate heavy metal ion sensing thanks to the follow-up of the chiral response of the NPs while interacting with the targeted ions. The detection limits and sensitivity are then sensed *via* CD spectra since CD signals are quenched with increasing metal ion concentration. In addition, compared to conventional CdSe quantum dots or quantum rods, 2D CdSe NPLs with few layers exhibit unique absorption and emission properties, including extremely narrow and separated absorption peaks resulting from heavy and light hole excitations.

Herein, we synthesized cysteine-capped four layer CdSe NPLs *via* an appropriate ligand exchange reaction between oleate anions and chiral cysteine molecules. The chirality transfer was monitored *via* electronic CD measurements and the chiral genesis was investigated through theoretical modelling based on the density functional theory (DFT). Finally, the as-synthesized chiral CdSe NPLs were applied as a chiral probe to detect lead ions, and it shows high sensitivity with a LOD close to 4.9 nM. The strong interaction between the thiol groups and lead ions results in a high selectivity for chiral sensing among seven kinds of metal ions. The linear relationship between the CD intensity, the *g*-factor and the ion concentrations demonstrates an ultrasensitive lead ion detection based on such a system. These results facilitate scalable chir-optical semiconductor nanostructures toward potential applications in chiral sensing, chiral separation and design of chiral devices.

Results and discussion

First, zinc blende (ZB) CdSe two-dimensional (2D) NPLs were synthesized directly from cadmium myristate, during which oleic acid (OA) was used as the capping agent to avoid aggregation. The CdSe NPLs with few atomic layers were prepared by precursor self-assembling followed by successive purification processes (Fig. 1). The transmission electron microscopy (TEM) image (Fig. 1b) presents the 2D morphology of NPLs with an average size of 5.1 ± 1.4 nm in width and 25.1 ± 2.7 nm in length (Fig. S1†). Fig. 1c shows the high-resolution TEM image, where the 3.23 Å lattice spacing corresponding to the (111) adjacent plane for the ZB crystal structure can be clearly seen. The powder X-ray diffraction (XRD) patterns also indicate that the CdSe NPLs are in the ZB phase. Fig. 1d shows sharp reflections at 2θ = 25°, 42° and 49°, which can be assigned to the (111), (220) and (311) planes of the ZB phase, respectively. The results are consistent with previous reports, which demonstrate the appropriate growth of CdSe NPLs.[57]

The most intriguing properties of 2D NPLs could be attributed to their unique optical response. The absorption spectrum of CdSe NPLs capped with OA (Fig. 2d) exhibits two sharp exci-

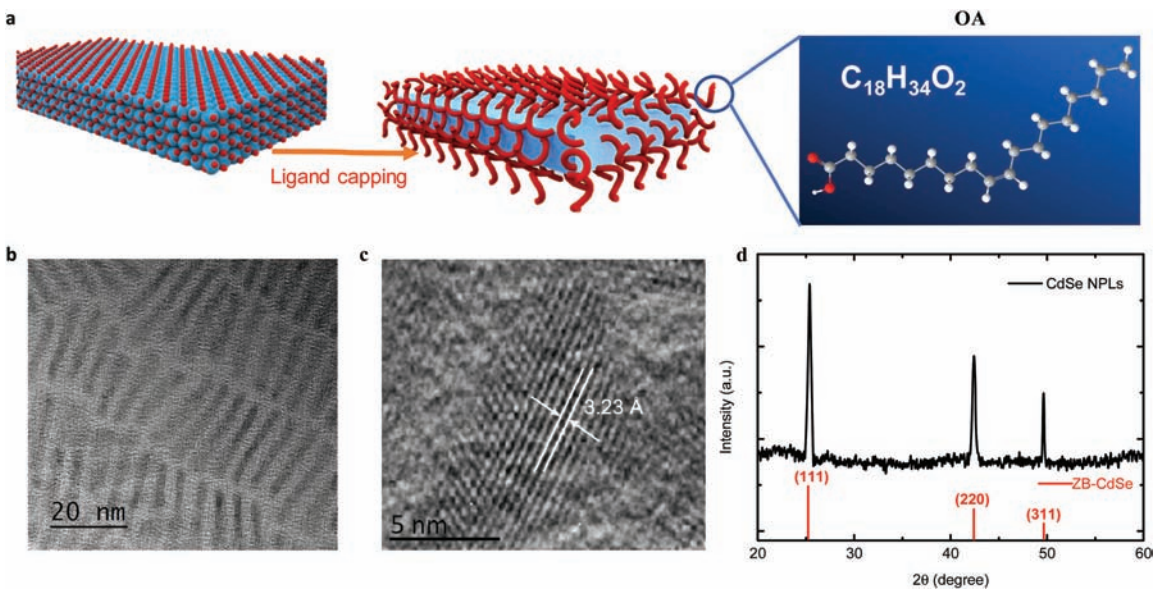

Fig. 1 (a) Schematic of the ligand capping of CdSe NPLs with oleic acid. (b) TEM and (c) HRTEM images of OA capped CdSe NPLs. (d) XRD spectra of CdSe NPLs.

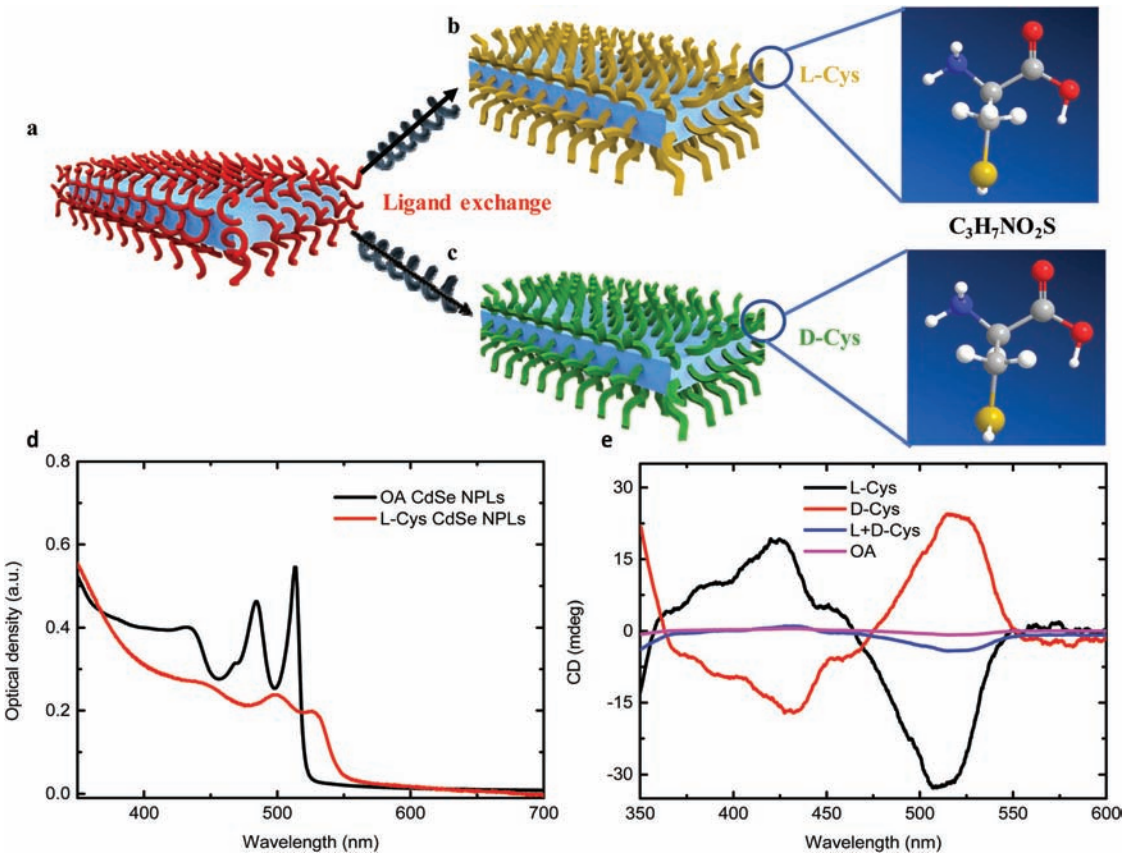

Fig. 2 (a–c) Ligand exchange process for phase transformation from oil to water with cysteine ligand replacement. (d) UV-Vis absorption spectra of CdSe NPLs before and after ligand exchange. (e) Chirality performance using electronic CD measurements for OA, L- and D-cys as well as L + D (ee = 0) mixed capped NPLs.

tonic peaks located at 484 and 513 nm. These two excitonic transitions are induced by different recombinations, namely the light hole–electron recombination for higher energy, and the heavy hole–electron recombination for lower energy absorption. The full widths at half maximum (FWHM) are 14 and 9 nm for light and heavy hole bands, respectively. The extremely narrow peaks are attributed to the strong quantum confinement effect in ultrathin 2D nanostructures. The observed absorption peaks indicate that the thickness of NPLs herein is around four monolayers according to previous studies.[36,58]

After the preparation and characterization of OA-capped NPLs, the subsequent ligand exchange reaction was performed using either the L- or D-form of the chiral cysteine (Fig. S2†). Due to the thiol groups in cysteine molecules, a strong Cd–S bond is formed and replaces the pre-existing interaction of the CdSe surface with OA molecules (Fig. 2a and c). After the ligand exchange, the morphology of the CdSe NPLs is maintained (Fig. S3†), and a red-shift in the absorption spectrum for both light and heavy hole–electron transitions is observed to 498 and 528 nm respectively. The red-shift originates from the partial delocalization of the carrier wave function from the NPLs to the ligands.[36] Besides, the evident broadening of the two excitonic peaks demonstrates the change of ligand density, as well as the dipole–dipole coupling after the ligand exchange and the new aqueous dispersion.

Electronic CD measurements were then performed to investigate the chiroptical response of the cysteine functionalized CdSe NPLs. Indeed, a bipinnate appearance of CD signals with multiple peaks arises in the vicinity of the exciton absorption of the NPLs, and a nearly mirrored CD line-shape is recorded when L- and D-cys are used as surface ligands respectively (Fig. 2e, black and red lines). Whereas in contrast, when an achiral ligand (OA) or an equal amount of each enantiomer of cysteine (enantiomer excess, ee = 0) is used, the CD observations exhibit weak or even silent responses (pink and blue lines). All these results indicate that the induced chiroptical properties are mainly attributed to the chirality transfer from the chiral surface ligand to the achiral semiconductor core. Specifically, at the band-edge position close to 520 nm, the obtained CD shows the strongest value of the signal with an anisotropy factor close to 3×10^{-4}, which is in good agreement with previous studies.[15,19]

To clarify the CD line shape and the chirality transfer mechanisms in these NPL nanostructures, simulations about the molecular structure and orbital wave function in hybrid systems based on the TD-DFT method were performed. The ground state geometries of L-cys and D-cys capped CdSe nano-

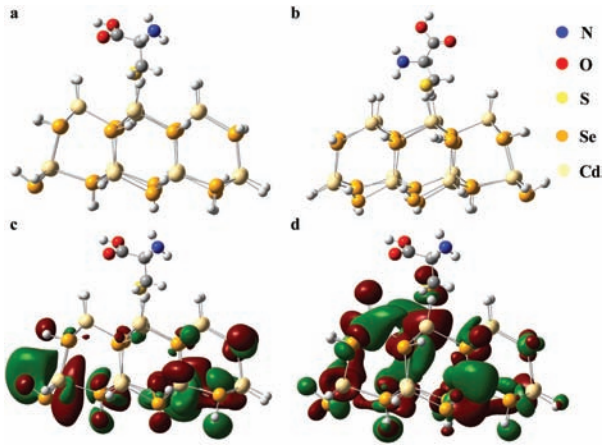

Fig. 3 (a) L- (b) D-cys capped CdSe nanocluster with optimized geometries. (c) Calculated frontier molecular orbitals of the LUMO and (d) HOMO for the L-cys capped CdSe nanocluster.

clusters are shown in Fig. S4.† Fig. 3a and b illustrate the optimized ground state geometries of L-cys and D-cys capped CdSe nanoclusters, which were utilized as the prototypes with much smaller sizes than in reality. All the calculations were conducted in the red hat linux system. We incorporated four ligands into the bare CdSe nanocluster with the ZB crystal structure. For the chiral activity transfer mechanism, the surface chiral ligand would hybridize with the electronic state of the achiral inorganic nanoparticle core (the excitonic band in this system), leading to the strong wave function overlap in orbital coupling. The calculated frontier molecular orbitals hybridized in the lowest unoccupied molecular orbitals (LUMO) and the highest occupied molecular orbitals (HOMO) for the L-cys capped CdSe nanocluster are shown in Fig. 3c and d. The HOMO showing strong wave function overlaps between the ZB CdSe nanocluster and the thiol group in the chiral ligand could be clearly observed. The results demonstrate the delocalized orbitals in CdSe and cysteine in the organic ligand capped complexes. In contrast, the LUMO exhibits missing overlaps of the wave function of the nanocluster and chiral ligands. Fig. S5† shows a similar electronic state coupling tendency for the HOMO−1 to HOMO−3 and LUMO+1 to LUMO+3. These observations are consistent with the previous simulation results for CdSe quantum dots and quantum rods.[19,34] Therefore, the intrinsic chirality of bare nanoclusters were ruled out. The induction of chirality onto the achiral

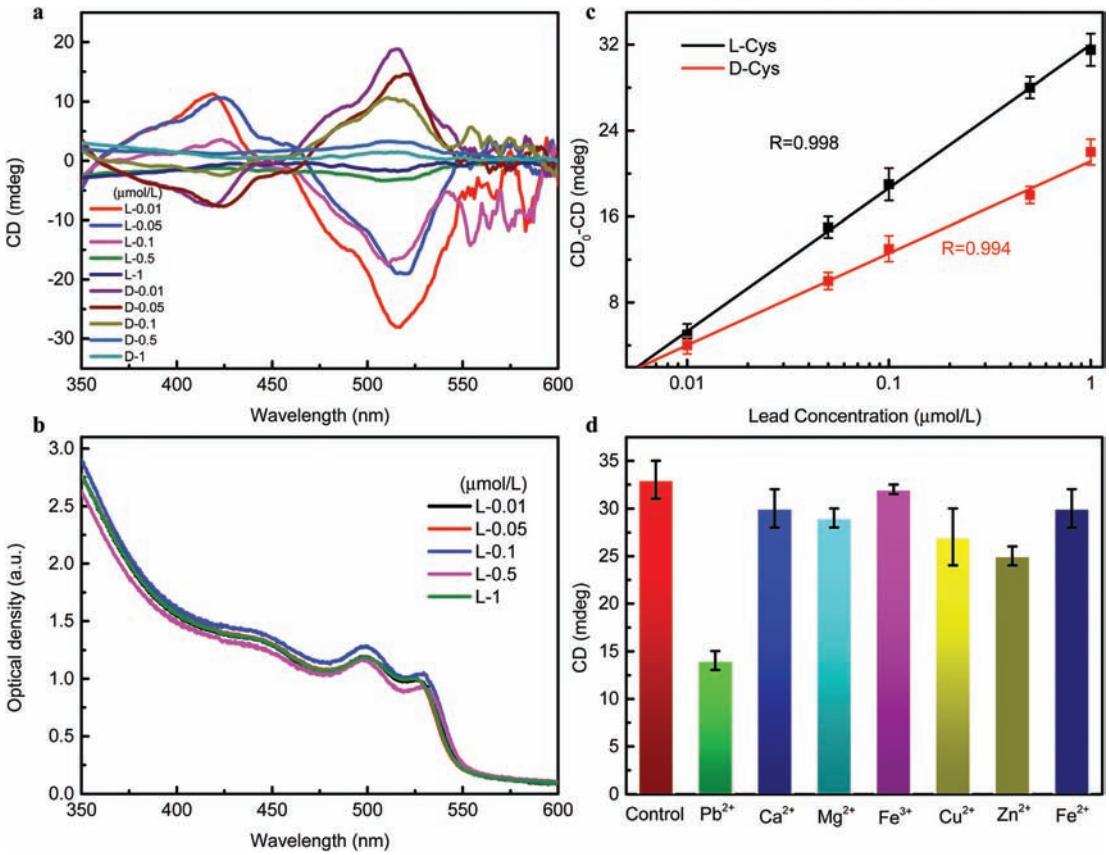

Fig. 4 (a) CD and (b) absorption measurements for lead ion detection ranging from 0.01 to 1 μM, both for L- and D-cys capped NPLs. (c) linear relationship between the chiral signal at 520 nm and various lead ion concentrations. (d) Examination of the high selectivity of the CdSe NPL chiral sensor with seven kinds of metal ion target analytes, the concentrations of all metal ions are set at 0.1 μM. Statistics were performed on at least 5 times for the control at an OD of 1.2 and 3 times for each ion.

CdSe nanocluster could then be ascribed to the orbital coupling effect.

Based on the above discussions, it is noted that the chirality of the NPLs is due to the introduction of the chiral ligand. The affinity of lead for sulfur is such that once the external lead ions are introduced, the Pb–S bonding forms reducing the amount of chiral cysteine linked to the CdSe NPL surface and inducing a quenching of the CD signal. The higher concentration of lead ions then results in a larger chiral signal quenching through weakening the electron state interaction between cysteine and CdSe NPLs. This provides a possible prerequisite for the construction of highly sensitive heavy metal ion sensing. In this work, we utilized lead(II) phosphate, $Pb_3(PO_4)_2$, as the lead source for detection. All the aqueous analyte samples were adjusted to the pH = 10 environment. Fig. 4a shows the CD peak response after adding various concentrations of lead ions. Their chiroptical activity showed a significant decrease with increasing lead ion concentrations. The CD intensity around 520 nm in L-cys capped CdSe NPLs decreased from 20 mdeg to less than 1 mdeg at a lead ion concentration between 0.01 and 1 μM. Similarly, the D-cys capped NPLs show a signal decrease from 27 mdeg to less than 1 mdeg with the same ion concentration procedures. The UV-vis absorption spectra in the meantime only exhibit a slight variation of the absorption intensity with the same ion concentration inductions (Fig. 4b). Fig. 4c reveals that chiral NPLs exhibit a clear linear relationship of CD intensity response at 520 nm *versus* the logarithmic lead ion concentration in the range of 0.01 to 1 μM, with correlation coefficients of 0.998 and 0.994 for L- and D-cys capped NPLs, respectively. The LOD for lead ion sensing is determined to be 4.9 ± 0.3 nM, from the straight line obtained in Fig. 4c.

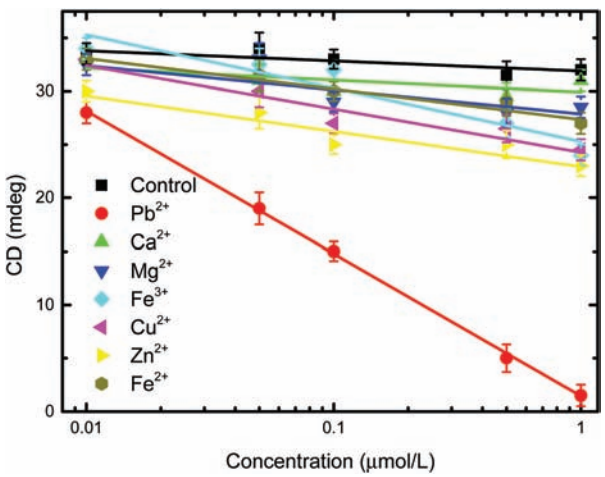

Fig. 5 Relationship between the CD intensity and ion concentrations for the seven kinds of metal ions.

Due to the similar absorption curve irrespective of the various lead ion amounts, the *g*-factor does also show a similar linear relationship and chiral sensor performance (Fig. S6†). The *g* values for L-cys NPL detection decrease from 2.8×10^{-4} to 1.59×10^{-5}, with an ion concentration increase from 0.01 to 1 μM. Similarly, the relevant *g* values of the D-cys sensor decrease from 1.87×10^{-4} to 1.51×10^{-5} in the same Pb concentration range. The correlation coefficient achieves 0.998 and 0.994 for L and D-cys samples, respectively. These results demonstrate that the lead ion did significantly affect the chiral configurations. The pre-existing Cd–S bonds were destroyed, thereby resulting in the stripping of the stabilizing ligand. The newly formed spatial configuration blocks the chirality transfer from the ligand to the surface of inorganic cores. The chiroptical activity then gradually decreases with the ligand peeling off until becoming null, since it originated from chirality transfer from the ligand.

To probe the specificity of the lead ion detection, we prepared a large enough quantity of NPL starting material in one single batch to be able to also test six other metal ions at a 0.1 μM concentration for a comparison purpose. As shown in Fig. 4d, compared to the control sample (CD intensity at around 520 nm (L-cys capped NPLs) 33 mdeg), the addition of Ca^{2+}, Mg^{2+}, Fe^{3+}, and Fe^{2+} resulted in the decrease of CD intensity in different extents in a range less than 15% of the control. The L-cys capped NPL solutions seemed to be a bit more sensitive to the addition of Cu^{2+} and Zn^{2+} with respective decreases of 18 and 25% of CD signals compared to the ion free control sample. Remarkably, among all the ions, the lead ions lead to the strongest CD signal quenching (58%) of the intensity of

Table 1 Lead ions' limit of detection (LOD) and linear range

Sensing system	Detected metal ions	Range (M) (Pb)	LOD (M) (Pb)	Ref.
Au nanoparticles	Pb, Fe, Mn *etc.*	1.0×10^{-7}–1.0×10^{-5}	1.0×10^{-7}	59
CdTe-TGA QDs	Pb	2.0×10^{-6}–1.0×10^{-4}	2.7 × 10−7	55
Graphene oxide	Pb, K, Cu *etc.*	5.0×10^{-9}–3.0×10^{-7}	3.0×10^{-9}	60
CdZnSe-GSH QDs	Pb, Zn, Co *etc.*	5.0×10^{-9}–2.0×10^{-5}	2.7×10^{-7}	56
CdSe-DAB QDs	Cd, Pb, Mg *etc.*	1.0×10^{-5}–1.5×10^{-4}	6.0×10^{-5}	54
CdSe/CdS-XO QDs	Pb, Cu *etc.*	5.0×10^{-8}–6.0×10^{-6}	2.2×10^{-8}	53
CdTe-TGA QDs	Pb, Zn, Co *etc.*	2.0×10^{-8}–3.6×10^{-6}	8.0×10^{-8}	52
GSH-Mn-ZnS QDs	Pb, Na, Cd *etc.*	4.8×10^{-9}–4.8×10^{-7}	2.2×10^{-9}	51
MPA-Mn-ZnS QDs	Pb, Mg, Zn *etc.*	4.0×10^{-8}–6.0×10^{-6}	3.7×10^{-8}	50
CdSe-Cys NPLs	Pb, Fe, Cu *etc.*	1.0×10^{-8}–1.0×10^{-6}	4.9×10^{-9}	This work

TGA: Thioglycolic acid; GSH: glutathione; DAB: diaminobutane-based poly(propyleneimine) dendrimers; XO: xylenol orange; MPA: mercaptopropionic acid; Cys: cysteine.

the control sample. A summary of the relationship between the CD intensity *versus* ion concentrations for the seven kinds of metal ions is shown in Fig. 5. The expected linear relationship significant of an effective sensing ability is present only in the case of lead ion detection. The slopes of fitted curves are summarized in Table S1.† These evaluations indicate that the CdSe NPLs capped with the chiral ligand are appropriate only for lead ion detection with both specificity and selectivity. As summarized in Table 1, our chiral detected performance was comparable to (or even better than) the conventional optical heavy or non-metal ion sensor based on photoluminescence methods. The CdSe NPLs could not be used for detecting lead ions through photoluminescence methods due to the non-luminous behavior after ligand exchange. However, the ion detection process could be realized through CD spectrum detection. Our work then provides a new and simple strategy for these non-luminous semiconductors in the field of heavy metal ion detection.

Conclusions

In summary, ultrathin CdSe NPLs with four monolayers were prepared in this work. Ligand exchange treatment was conducted to achieve aqueous cysteine capped NPLs. The chiral ligand induced the chiroptical activity unlocking the excitonic transition peaks of CdSe NPLs. Moreover, we have discussed the chiral signal that originated from the ligand transfer mechanism according to the orbital coupling simulation based on the TD-DFT calculation. Taking advantage of this mechanism, highly sensitive chiroptical sensing for lead ion detection with high selectivity was demonstrated. These results revealed that such chiral super-nanostructures may serve as a versatile platform for heavy metal ion detection in waste water processes.

Experimental section

Materials

Cadmium nitrate tetrahydrate ($Cd(NO_3)_2{\cdot}4H_2O$, 99.997%), cadmium acetate dihydrate ($Cd(Ac)_2{\cdot}2H_2O$, 98.0%), oleic acid (OA, 90%), and tetramethylammonium hydroxide pentahydrate (TMAH, ≥97%) were purchased from Sigma-Aldrich. L-Cysteine hydrochloride monohydrate (99%), D-cysteine hydrochloride monohydrate (98%), and selenium powder (Se, ≥99.999%) were purchased from Aladdin. 1-Octadecene (ODE, 90%) and sodium myristate (98%) were purchased from J & K. Pure water was purchased from Wahaha, China. All chemicals were used as received without further purification.

Preparation of cadmium myristate

Cadmium myristate was prepared according to the recipe given in the literature. For a typical synthesis, 1.23 g of $Cd(NO_3)_2{\cdot}4H_2O$ was dissolved in 40 mL of methanol and 3.13 g of sodium myristate was dissolved in 250 mL of methanol. After complete dissolution of $Cd(NO_3)_2{\cdot}4H_2O$ and sodium myristate powders, solutions were mixed and stirred vigorously around 1 h. Then, the cadmium myristate ($Cd(myristate)_2$) powders were precipitated by centrifugation and re-dispersed in methanol. The washing step with methanol was performed at least three times to remove any unreacted and/or excess precursors. After successive washing steps, the precipitated part was completely dried under vacuum overnight.

Synthesis of the CdSe core NPLs

CdSe nanoplatelets (NPLs) having four monolayers (4 MLs) were prepared according to the procedure described in the literature with little modifications.[61] For a typical synthesis, 0.17 g (0.3 mmol) of $Cd(myristate)_2$, 0.012 g (0.15 mmol) of Se and 15 mL of ODE were introduced into a three-neck flask. The solution was degassed at 100 °C for an hour under vacuum. After the degassing step, the solution was heated to 240 °C under an argon atmosphere and 0.055 g (0.2 mmol) of $Cd(Ac)_2{\cdot}2H_2O$ was swiftly added to the reaction solution. After 10 min growth at 240 °C, 1 mL of OA was injected, and the temperature of the solution was decreased to room temperature. The cadmium precursor injection temperature and the growth time were found to be important for the resulting shape and size of the CdSe core NPLs.

The resulting 4 ML CdSe NPLs are separated from other reaction products with successive purification steps. First, the resulting mixture is centrifuged at 14 500 rpm for 10 min, and the supernatant is removed from the centrifuge tube. The precipitate is dried under nitrogen, re-dispersed in hexane, and centrifuged again at 4500 rpm for 5 min. In the second step, the supernatant is separated into another centrifuge tube, and 30% ethanol is added into the supernatant solution. In the last step, after the turbid solution is centrifuged at 4500 rpm for 5 min, the precipitate is dissolved in hexane and filtered with a 0.20 μm filter.

Ligand exchange of the CdSe NPLs with chiral cysteine molecules

The L- and D-cysteine ligand exchange was carried out using a previously reported method.[19,36] D- or L-cysteine hydrochloride monohydrate (0.2 M) was dissolved in DI water. The pH of the solution was adjusted to 12 by TMAH to form the cysteine solution. 2 mL hexane solution containing CdSe NPLs was added into 2 ml of cysteine solution. The mixture was stirred at room temperature for 24 h. The reaction mixture was left to stand for 1 h to allow the phases to separate. The bottom aqueous layer was removed with a syringe, and the Cys-CdSe NPLs were purified by precipitation with ethanol/DI water (4 : 1, two times). The purified Cys-NPLs were re-dispersed in DI H_2O and stored at room temperature in the dark (O.D. = 0.26 for 2 mm optical length after ligand exchange).

Structural and optical characterization

The UV/vis absorption measurements were performed using a TU-1901 double-beam UV/vis spectrophotometer (Beijing Purkine General Instrument Co. Ltd, China), and the emission

spectra were recorded on a fluoroSENS spectrophotometer (Gilden Photonics).

CD measurements

CD measurements were conducted on a JASCO J-1500 CD spectrometer at a scan rate of 20 nm min^{-1}. All CD experiments were carried out in Milli-Q water with a quartz cuvette (1 cm path length, Hellma). TEM images were collected using a Tecnai F30 microscope working at 300 kV. Powder X-ray diffraction (XRD) was carried out in a Rigaku Smartlab system.

All the samples were at concentrations leading to a peak absorbance of 1.15 O.D.

Calculation of the *g*-factor

In designing chiral nanoparticles for application, the anisotropy or *g*-factor is a key parameter to determine the optical activity due to its easy determination by comparing the CD spectrum with the absorption spectrum. The equation is as follows: $g = \theta/3.298 \times 10^4 \times A$, where θ is the vertical coordinate of the CD spectrum, and A is the value in the absorption spectrum at the same concentration used to measure the CD spectrum.

Simulation method

Gaussian 09 software is used for all chemical calculations. Ground state geometries were optimized at the DFT level. UV and CD spectra were calculated with TD-DFT. B3LYP and LanL2DZ basis sets were used for all the elements in the calculations. The small CdSe clusters usually are in the form of a tetrahedron; herein, we constructed a tetrahedron-like Cd_4Se_9 cluster to mimic the interactions between the chiral light and the nanoplatelets. We take the charge states of Cd and Se as 2^+ and 2^-. All the geometries were optimized during modeling in accordance with the principle of the lowest energy.[62–68]

Conflicts of interest

The authors declare no competing financial interest.

Acknowledgements

This work is supported by the National Natural Science Foundation of China (11574130) and the Shenzhen Science and Technology Innovation Commission (project no. KQJSCX20170726145748464, JCYJ20150930160634263, JCYJ20170302142433007, JCYJ20170818103918295 and KQTD2015071710313656).

References

1 J. Cheng, E. H. Hill, Y. Zheng, T. He and Y. Liu, *Mater. Chem. Front.*, 2018, **2**, 662.
2 W. Ma, L. G. Xu, A. F. de Moura, X. L. Wu, H. Kuang, C. L. Xu and N. A. Kotov, *Chem. Rev.*, 2017, **117**, 8041.
3 A. Ben-Moshe, B. Maoz, A. O. Govorov and G. Markovich, *Chem. Soc. Rev.*, 2013, **42**, 7028.
4 C. Noguez and I. L. Garzon, *Chem. Soc. Rev.*, 2009, **38**, 757.
5 T. Cao and M. J. Cryan, *J. Opt.*, 2012, **14**, 085101.
6 T. Cao, Y. Li, X. Zhang and Y. Zou, *Photonics Res.*, 2017, **5**, 441.
7 T. Cao, L. Mao, Y. Qiu, L. Lu, A. Banas, K. Banas, R. E. Simpson and H.-C. Chui, *Adv. Opt. Mater.*, 2019, **7**, 1801172.
8 T. Cao and Y. Qiu, *Nanoscale*, 2018, **10**, 566.
9 T. Cao, C.-W. Wei, L.-B. Mao and S. Wang, *Opt. Express*, 2015, **23**, 18620.
10 C. Hao, L. Xu, M. Sun, W. Ma, H. Kuang and C. Xu, *Adv. Funct. Mater.*, 2018, **28**, 1802372.
11 W. Ma, P. Fu, M. Sun, L. Xu, H. Kuang and C. Xu, *J. Am. Chem. Soc.*, 2017, **139**, 11752.
12 M. Sun, T. Hao, X. Li, A. Qu, L. Xu, C. Hao, C. Xu and H. Kuang, *Nat. Commun.*, 2018, **9**, 4494.
13 M. Sun, L. Xu, A. Qu, P. Zhao, T. Hao, W. Ma, C. Hao, X. Wen, F. M. Colombari, A. F. de Moura, N. A. Kotov, C. Xu and H. Kuang, *Nat. Chem.*, 2018, **10**, 821.
14 H. Y. Ye, Y. Y. Tang, P. F. Li, W. Q. Liao, J. X. Gao, X. N. Hua, H. Cai, P. P. Shi, Y. M. You and R. G. Xiong, *Science*, 2018, **361**, 151.
15 M. V. Mukhina, V. G. Maslov, A. V. Baranov, A. V. Fedorov, A. O. Orlova, F. Purcell-Milton, J. Govan and Y. K. Gun'ko, *Nano Lett.*, 2015, **15**, 2844.
16 A. S. Baimuratov, I. D. Rukhlenko, Y. K. Gun'ko, A. V. Baranov and A. V. Fedorov, *Nano Lett.*, 2015, **15**, 1710.
17 A. Ben-Moshe, A. O. Govorov and G. Markovich, *Angew. Chem., Int. Ed.*, 2013, **52**, 1275.
18 Y. W. Li, J. J. Cheng, J. G. Li, X. Zhu, T. C. He, R. Chen and Z. K. Tang, *Angew. Chem., Int. Ed.*, 2018, **57**, 10236.
19 J. J. Cheng, J. J. Hao, H. C. Liu, J. G. Li, J. Z. Li, X. Zhu, X. D. Lin, K. Wang and T. C. He, *ACS Nano*, 2018, **12**, 5341.
20 T. Nakashima, Y. Kobayashi and T. Kawai, *J. Am. Chem. Soc.*, 2009, **131**, 10342.
21 S. D. Elliott, M. P. Moloney and Y. K. Gun'ko, *Nano Lett.*, 2008, **8**, 2452.
22 W. C. Feng, J. Y. Kim, X. Z. Wang, H. A. Calcaterra, Z. B. Qu, L. Meshi and N. A. Kotov, *Sci. Adv.*, 2017, **3**, e1601159.
23 J. J. Cheng, G. Le Saux, J. Gao, T. Buffeteau, Y. Battie, P. Barois, V. Ponsinet, M. H. Delville, O. Ersen, E. Pouget and R. Oda, *ACS Nano*, 2017, **11**, 3806.
24 Y. L. Zhou, R. L. Marson, G. van Anders, J. Zhu, G. X. Ma, P. Ercius, K. Sun, B. Yeom, S. C. Glotzer and N. A. Kotov, *ACS Nano*, 2016, **10**, 3248.
25 J. Yeom, B. Yeom, H. Chan, K. W. Smith, S. Dominguez-Medina, J. H. Bahng, G. P. Zhao, W. S. Chang, S. J. Chang, A. Chuvilin, D. Melnikau, A. L. Rogach, P. J. Zhang, S. Link, P. Kral and N. A. Kotov, *Nat. Mater.*, 2015, **14**, 66.
26 B. Xu, P. He, H. Liu, P. Wang, G. Zhou and X. Wang, *Angew. Chem., Int. Ed.*, 2014, **53**, 2339.
27 E. D. Sone, E. R. Zubarev and S. I. Stupp, *Angew. Chem., Int. Ed.*, 2002, **41**, 1705.

28 S. Jiang, M. Chekini, Z. B. Qu, Y. C. Wang, A. Yeltik, Y. G. Liu, A. Kotlyar, T. Y. Zhang, B. Li, H. V. Demir and N. A. Kotov, *J. Am. Chem. Soc.*, 2017, **139**, 13701.

29 Y. H. Shi, P. F. Duan, S. W. Huo, Y. G. Li and M. H. Liu, *Adv. Mater.*, 2018, **30**, 1705011.

30 G. V. Naik, V. M. Shalaev and A. Boltasseva, *Adv. Mater.*, 2013, **25**, 3264.

31 M. Puri and V. E. Ferry, *ACS Nano*, 2017, **11**, 12240.

32 F. Purcell-Milton, A. K. Visheratina, V. A. Kuznetsova, A. Ryan, A. O. Orlova and Y. K. Gunko, *ACS Nano*, 2017, **11**, 9207.

33 J. K. Choi, B. E. Haynie, U. Tohgha, L. Pap, K. W. Elliott, B. M. Leonard, S. V. Dzyuba, K. Varga, J. Kubelka and M. Balaz, *ACS Nano*, 2016, **10**, 3809.

34 U. Tohgha, K. K. Deol, A. G. Porter, S. G. Bartko, J. K. Choi, B. M. Leonard, K. Varga, J. Kubelka, G. Muller and M. Balaz, *ACS Nano*, 2013, **7**, 11094.

35 X. Q. Gao, X. W. Zhang, K. Deng, B. Han, L. Y. Zhao, M. H. Wu, L. Shi, J. W. Lv and Z. Y. Tang, *J. Am. Chem. Soc.*, 2017, **139**, 8734.

36 G. L. Yang, M. Kazes and D. Oron, *Adv. Funct. Mater.*, 2018, **28**, 1802012.

37 T. Stauber, T. Low and G. Gomez-Santos, *Phys. Rev. Lett.*, 2018, **120**, 046801.

38 F. Purcell-Milton, R. McKenna, L. J. Brennan, C. P. Cullen, L. Guillemeney, N. V. Tepliakov, A. S. Baimuratov, I. D. Rukhlenko, T. S. Perova, G. S. Duesberg, A. V. Baranov, A. V. Fedorov and Y. K. Gun'ko, *ACS Nano*, 2018, **12**, 954.

39 X. Gao, X. Zhang, L. Zhao, P. Huang, B. Han, J. Lv, X. Qiu, S.-H. Wei and Z. Tang, *Nano Lett.*, 2018, **18**, 6665.

40 X. A. Wang and Z. Y. Tang, *Small*, 2017, **13**, 1601115.

41 S. M. Morrow, A. J. Bissette and S. P. Fletcher, *Nat. Nanotechnol.*, 2017, **12**, 410.

42 X. Lan and Q. B. Wang, *Adv. Mater.*, 2016, **28**, 10499.

43 C. Hao, L. Xu, W. Ma, X. Wu, L. Wang, H. Kuang and C. Xu, *Adv. Funct. Mater.*, 2015, **25**, 5816.

44 I. V. Martynenko, V. A. Kuznetsova, I. K. Litvinov, A. O. Orlova, V. G. Maslov, A. V. Fedorov, A. Dubavik, F. Purcell-Milton, Y. K. Gun'ko and A. V. Baranov, *Nanotechnology*, 2016, **27**, 075102.

45 M. Matuschek, D. P. Singh, H. H. Jeong, M. Nesterov, T. Weiss, P. Fischer, F. Neubrech and N. Liu, *Small*, 2018, **14**, 1702990.

46 Z. Y. Bao, W. Zhang, Y. L. Zhang, J. J. He, J. Y. Dai, C. T. Yeung, G. L. Law and D. Y. Lei, *Angew. Chem., Int. Ed.*, 2017, **56**, 1283.

47 M. V. Mukhina, I. V. Korsakov, V. G. Maslov, F. Purcell-Milton, J. Govan, A. V. Baranov, A. V. Fedorov and Y. K. Gun'ko, *Sci. Rep.*, 2016, **6**, 24177.

48 Y. H. Xia, Y. L. Zhou and Z. Y. Tang, *Nanoscale*, 2011, **3**, 1374.

49 K. M. Mayer and J. H. Hafner, *Chem. Rev.*, 2011, **111**, 3828.

50 T. T. Gan, N. J. Zhao, G. F. Yin, M. D. Tu, J. G. Liu and W. Q. Liu, *New J. Chem.*, 2017, **41**, 13425.

51 J. L. Chen, Y. X. Zhu and Y. Zhang, *Spectrochim. Acta, Part A*, 2016, **164**, 98.

52 S. Xu, S. H. Xu, Y. S. Zhu, W. Xu, P. W. Zhou, C. Y. Zhou, B. Dong and H. W. Song, *Nanoscale*, 2014, **6**, 12573.

53 Q. Zhao, X. L. Rong, L. Chen, H. B. Ma and G. H. Tao, *Talanta*, 2013, **114**, 110.

54 M. Algarra, B. B. Campos, B. Alonso, M. S. Miranda, A. M. Martinez, C. M. Casado and J. C. G. Esteves da Silva, *Talanta*, 2012, **88**, 403.

55 H. M. Wu, J. G. Liang and H. Y. Han, *Microchim. Acta*, 2008, **161**, 81.

56 E. M. Ali, Y. G. Zheng, H. H. Yu and J. Y. Ying, *Anal. Chem.*, 2007, **79**, 9452.

57 Y. Kelestemur, M. Olutas, S. Delikanli, B. Guzelturk, M. Z. Akgul and H. V. Demir, *J. Phys. Chem. C*, 2015, **119**, 2177.

58 S. Ithurria, M. D. Tessier, B. Mahler, R. P. S. M. Lobo, B. Dubertret and A. Efros, *Nat. Mater.*, 2011, **10**, 936.

59 F. Chai, C. A. Wang, T. T. Wang, L. Li and Z. M. Su, *ACS Appl. Mater. Interfaces*, 2010, **2**, 1466.

60 Y. F. Bai, L. Zhao, Z. H. Chen, H. Y. Wang and F. Feng, *Anal. Methods*, 2014, **6**, 8120.

61 Y. Kelestemur, B. Guzelturk, O. Erdem, M. Olutas, K. Gungor and H. V. Demir, *Adv. Funct. Mater.*, 2016, **26**, 3570.

62 A. N. Beecher, X. H. Yang, J. H. Palmer, A. L. LaGrassa, P. Juhas, S. J. L. Billinge and J. S. Owen, *J. Am. Chem. Soc.*, 2014, **136**, 10645.

63 T. Vossmeyer, G. Reck, L. Katsikas, E. T. K. Haupt, B. Schulz and H. Weller, *Science*, 1995, **267**, 1476.

64 C. T. Lee, W. T. Yang and R. G. Parr, *Phys. Rev. B: Condens. Matter Mater. Phys*, 1988, **37**, 785.

65 W. R. Wadt and P. J. Hay, *J. Chem. Phys.*, 1985, **82**, 284.

66 P. J. Hay and W. R. Wadt, *J. Chem. Phys.*, 1985, **82**, 299.

67 P. J. Hay and W. R. Wadt, *J. Chem. Phys.*, 1985, **82**, 270.

68 M. J. Frisch, G. W. Trucks, H. B. Schlegel, G. E. Scuseria, M. A. Robb, J. R. Cheeseman, G. Scalmani, V. Barone, G. A. Petersson, H. Nakatsuji, X. Li, M. Caricato, A. Marenich, J. Bloino, B. G. Janesko, R. Gomperts, B. Mennucci, H. P. Hratchian, J. V. Ortiz, A. F. Izmaylov, J. L. Sonnenberg, D. Williams-Young, F. Ding, F. Lipparini, F. Egidi, J. Goings, B. Peng, A. Petrone, T. Henderson, D. Ranasinghe, V. G. Zakrzewski, J. Gao, N. Rega, G. Zheng, W. Liang, M. Hada, M. Ehara, K. Toyota, R. Fukuda, J. Hasegawa, M. Ishida, T. Nakajima, Y. Honda, O. Kitao, H. Nakai, T. Vreven, K. Throssell, J. A. Montgomery Jr., J. E. Peralta, F. Ogliaro, M. Bearpark, J. J. Heyd, E. Brothers, K. N. Kudin, V. N. Staroverov, T. Keith, R. Kobayashi, J. Normand, K. Raghavachari, A. Rendell, J. C. Burant, S. S. Iyengar, J. Tomasi, M. Cossi, J. M. Millam, M. Klene, C. Adamo, R. Cammi, J. W. Ochterski, R. L. Martin, K. Morokuma, O. Farkas, J. B. Foresman and D. J. Fox, *R. A. Gaussian 09*, Gaussian, Inc., Wallingford CT, 2016.